ON THE ROLE OF ALLOY COMPOSITION AND PROCESSING PARAMETERS IN NANOCLUSTER FORMATION AND DISPERSION STRENGTHENING IN NANOSTRUCTURED FERRITIC ALLOYS -

M. J. Alinger and G. R. Odette (University of California Santa Barbara) and D. T. Hoelzer (Oak Ridge National Laboratory)

OBJECTIVE

The objective of this research was to develop an understanding of the role of composition and processing parameters on nanofeature (NF) formation and dispersion strengthening in nanostructured ferritic alloys (NFA).

SUMMARY

An extensive experimental study to characterize the sequence-of-events that lead to the formation of a very high density of Y-Ti-O solute nanoclusters (NFs) in mechanically alloyed (MA), hot isostatically pressed (HIPed) ferritic stainless steels is reported. Yttria and O dissolve in the Fe-14Cr3W(0.4Ti) powders during MA. The dissolved Y and O, and when present Ti, subsequently precipitate during hot consolidation. The number densities and volume fractions of the NF decrease, and their radii increase, with increasing consolidation temperature. The NF form at 850 and 1000°C in both attritor and higher energy SPEX milled alloys containing Y, both with and without Ti additions. SPEX milling produces higher volume fractions of NFs and higher hardness in these cases. The presence of Ti refines the NFs, and both Ti and high milling energy (SPEX versus attritor) are necessary for the formation NFs at the highest consolidation temperatures of 1150°C. Microhardness trends closely mirror the effects of the compositional and processing variables on the NFs. However, the precise structure and composition of the NFs are not well understood. Indeed, their character varies, depending on the alloy composition and processing variables. The NFs appear to range from coherent solute enriched zones, or sub-oxides, to complex oxide phases.

PROGRESS AND STATUS

Introduction

The development of alloy systems for structural applications at elevated temperatures in high-energy neutron environments poses a complex materials challenge. Such alloys must manifest long-term stability of both their microstructure and mechanical properties. Microstructural stability includes the ability to successfully manage high levels of both transmutation product helium and excess vacancies and self-interstitial atom defects, that result from the displacement of atoms from their lattice positions, while also minimizing residual radioactivity. Additionally, advanced alloys must balance fracture toughness at lower temperatures with high creep strength at elevated temperatures. In combination, these requirements present a unique opportunity to use a materials science based approach to alloy design and development.

Pioneering work by Fisher [1] and researchers in the US breeder reactor program [2] in the nineteen eighties showed that mechanical alloying (MA) of Fe-14Cr-Ti-Mo powders with Y_2O_3, followed by hot consolidation, produces ultra fine, nm-scale precipitates or solute clusters that yield both high static and creep strength, as well as radiation damage resistance. Outstanding research to develop these alloys by Ukai and co-workers in Japan has continued up to the present [3-14].

Ukai et al. first recognized the importance of dissolved Ti in refining the Y_2O_3 precipitates [3], attributing this to reactions leading to the formation of Y_2TiO_5 oxides. Since then, various transmission electron microscopy techniques have been used to characterize NFA microstructures and to identify the Y-Ti-O features, typically at larger sizes of several nm [11, 15-23]. These studies have shown the presence of the pyrochlore complex oxide, $Y_2Ti_2O_7$, as well as Y_2TiO_5 and Y_2O_3 [9,11,17,18,20]. Mechanical property and TEM studies have also shown that the NFAs are resistant to radiation damage and that the Y-Ti-O features are both stable under irradiation and effective in trapping helium [2,22,24-30].

However, recent atom probe tomography (APT) studies [31-36] indicate that the smallest Y-Ti-O features differ from these complex oxides in that: a) their solute Ti plus Y metal to oxygen atom ratio is typically greater than 1; b) they have high to very high Ti to Y ratios up to 3/1, or more; and, in some cases, c) they may also contain considerable quantities of Fe. Small angle neutron scattering (SANS) measurements, which are a major focus of the work reported here, have shown that the nature of the Y-Ti-O features depends on the processing time-temperature history [37,38]. The SANS studies show that magnetic to nuclear scattering ratios and volume fractions of the Y-Ti-O features are also sometimes inconsistent with complex oxides, especially for processing paths with a slow ramp heat up to the nominal consolidation temperature. The APT and SANS results suggest that the smallest Y-Ti-O features may be sub-oxide, or even coherent GP zone-type, transition phases. Given this complexity, we will hereafter refer to the small, 1-3 nm diameter, Y-Ti-O features as nano-clusters (NFs).

Mechanical alloying also produces nanometer scale grain structures and high dislocation densities in the milled powders. The grains grow or recrystallize and the dislocations partially recover during hot consolidation, mainly depending on the processing temperature and the presence or absence NFs [12,19]. Hence, we will refer to these materials as nanostructured ferritic alloys (NFAs), to distinguish them from more conventional oxide dispersion strengthened (ODS) alloys, that generally contain coarser scale incoherent Y_2O_3 particles. The very high creep strength of NFAs has been attributed the presence NFs, although this remains to be fully demonstrated [2,3,9,14,28,39-41].

However, the effects of alloy composition and processing path on the sizes, number densities, volume fraction and basic character of NFs have not been well understood. The objective of this research was to develop a systematic knowledge base to guide processing to tailor microstructures and optimize the mechanical properties for particular applications. Specifically we will address the following two key questions:

1. What is the sequence-of-events leading to the formation of NFs?
2. What are the compositional and processing variables that control the characteristics of various types of NFs and other nm-scale features?

These questions were addressed by characterizing a set of model alloys, primarily using microhardness and SANS techniques. The model alloy powders were mechanically alloyed by ball milling and, with one exception, consolidated by hot isostatic pressing (HIPing) at temperatures from 850 to 1150°C. Other publications will address the time-temperature kinetics of formation of NFs, their thermal stability and their relation to alloy strength.

Experimental

Alloys

The series of model alloys used in this study represent variants of two commercial vendor NFAs, INCO 14Cr-Y-Mo-Ti-O MA957 and Kobe Steel 12Cr-Y-W-Ti-O, that we refer to as J12WYT. Both alloys contain Y equivalent to ≈ 0.25 to 0.30 wt.% Y_2O_3. These 12-14 wt.% Cr-Ti plus W or Mo alloys lie outside the γ-loop, hence, are classified as ferritic stainless steels, with good corrosion/oxidation resistance deriving from their high Cr content. The specific base model alloy composition used in this study is: 14 wt.% Cr, 3 wt. % W (a low activation replacement for Mo at mass ratio of about 2/1 to give approximately equal atomic fractions), 0.25 wt. % Y_2O_3 (note the Y in the alloy designations below generally refers to a Y_2O_3 source) and 0.4 wt% Ti. We refer to this base alloy composition alloy as U14YWT. The W provides solid solution strengthening, while Y, Ti and O collectively produce dispersion strengthening. Iron and yttrium are essentially immiscible, normally forming an intermetallic $Fe_{17}Y_2$ phase in dilute Y-Fe alloys. In the presence of dissolved O, Y_2O_3 (yttria) particles might be expected to replace $Fe_{17}Y_2$, simply based on their respective formation energies. Further, it might also be expected that the addition of Ti would lead to the formation of complex oxides, like $Y_2Ti_2O_7$ (pyrochlore) [42,43].

Table 1 shows the compositions of the model and commercial vendor alloys [38]. The model alloy matrix includes sequential additions of Ti, Y and O, where the latter two elements were introduced by ball milling elemental or alloyed powders with Y_2O_3 or metallic Y. The sequential solute addition matrix, described

further below, serves two main purposes. First, this approach allows determining the effects of both the individual and combinations of solutes on the hardness of NFAs. Second, the sequence of solute additions provides control alloys for SANS studies to evaluate to effect of a specific alloy modification on the NFs.

Table 1 The NFA Compositions (wt%) and Processing Parameters

Alloy ID	Alloy Element (wt%)							Milling	Consolidation	
	Cr	Ti	W	Y_2O_3	Al	Mo	Y	Technique	Process	Temperature(^oC)
MA957	14	1	-	0.30	-	0.3	-		Hot Ext.	1150
J12YWT	12	0.4	3	0.25	-	-	-		Hot Ext.	1150
PM2000	20	0.5	-	0.50	5.5	-	-		Hot Ext.	1150
U14Y	14	-	-	0.25	-	-	-	SPEX	HIP	850, 1000, 1150
U14YT	14	0.4	-	0.25	-	-	-	SPEX	HIP	850, 1000, 1150
U14YW	14	-	3	0.25	-	-	-	SPEX	HIP	850, 1000, 1150
U14YWT	14	0.4	3	0.25	-	-	-	SPEX	HIP	850, 1000, 1150
U14Y(M)T	14	0.4	-	-	-	-	0.2	SPEX	HIP	850, 1000, 1150
U14	14	-	-	-	-	-	-	SPEX	HIP	850, 1000, 1150
U14T	14	0.4	-	-	-	-	-	SPEX	HIP	850, 1000, 1150
U14W	14	-	3	-	-	-	-	SPEX	HIP	850, 1000, 1150
U14WT	14	0.4	3	-	-	-	-	SPEX	HIP	850, 1000, 1150
O14Y	14	-	-	0.25	-	-	-	Attritor	HIP	850, 1000, 1150
O14YT	14	0.4	-	0.25	-	-	-	Attritor	HIP	850, 1000, 1150
O14YWT	14	0.4	3	0.25	-	-	-	Attritor	HIP	850, 1000, 1150
O14YWTX	14	0.4	3	0.25	-	-	-	Attritor	Hot Ext.	850

The individual solute additions include Y, W and Ti. The paired additions include Y plus Ti, W plus Ti and W plus Y; the base alloy contains all three solutes, Y plus W plus Ti. One U14YT alloy, designated Y(M)T, was processed by milling the alloy powder with metallic Y, rather than Y_2O_3. As discussed below, all of these U-alloys were SPEX milled in small batches at the University of California Santa Barbara (UCSB). Table 1 also shows a series of alloys that were attritor milled at Oak Ridge National Laboratory (ORNL), designated by the letter O, with additions of Y, Y plus Ti and Y plus W plus Ti. Both U- and O-alloy powders were consolidated by HIPing at temperatures 850, 1000 and 1150°C. Finally, one O14YWT alloy, designated as O14YWTX, was extruded, rather than HIPed, at 850°C.

Mechanical Alloying

Iron and yttrium are essentially immiscible. Thus conventional melt processing techniques are not viable for dissolving Y into a Fe rich matrix. Further, even if Y could be dissolved in a Fe matrix, internal oxidation to form dispersed phases would be inhibited by Cr scales and low O solubility. Thus, one obvious approach to incorporating Y into Fe-rich matrix is mechanical alloying (MA) by ball milling Fe-rich alloy powders with yttria (Y_2O_3). Ball milling results in severe deformation and fragmentation mixing of fine powders by multiple energetic impacts between much larger hardened balls that are agitated to a significant kinetic energy by a variety of shaking processes. Two Y_2O_3 incorporation paths can be envisioned. In one case, the Y_2O_3 would be taken up in the metal powders as highly refined oxide fragments. The other possibility is that the Y_2O_3 is actually mechanically dissolved in the Fe-rich matrix by the combination of fragmentation and severe deformation. Highly supersaturated metallic solutions can be produced in this fashion [44]. The direct mixing-dissolution mechanism is not as obvious for brittle oxide powders. However, at small sizes, Y_2O_3 fragments might be diced to the atomic scale by a massive number of dislocation intersections. As shown later in this paper, the Y-O dissolution process appears to be dominant in the MA of Y_2O_3 with Fe-Cr-Ti powders. An excellent review of mechanical alloying can be found in Reference 45.

Two different methods for mechanical alloying iron-based powders with Y_2O_3 were used in this study: attritor milling (at ORNL) and the SPEX 8000 mixer-milling (at UCSB). The SPEX milling was performed in a stainless steel vial with hardened 0.95 cm diameter steel balls sealed in a dry argon atmosphere using a 10/1 ball to powder weight ratio (BWR). The powders were milled in 10 g batches for 8 h at ambient temperature with forced air-cooling. The attritor milling was also performed in an argon atmosphere in a water-cooled vessel, using ≈ 5 mm diameter steel balls with a 10/1 BWR. In this case the powders were milled for 80 h in 200 g batches. Note all steps involving powder handling were carried out in glove box with a dry Ar atmosphere.

Hot Consolidation

Both hot isostatic pressing (HIPing) and hot extrusion were used to consolidate the MA powders. In the case of HIPing, the powders were loaded in low carbon steel cans that were evacuated to 2.5×10^{-6} Torr and degassed at 300°C for 24 h prior to final weld sealing of a crimped exhaust tube. The various U-alloys in Table 1 were HIPed in 50 to 100 g batches. One HIP can typically contained a stack-up of 3 alloy powders separated by Y_2O_3 discs. The HIPing was performed at 200 MPa for 3h at 850, 1000 and 1150°C. The canned powders were ramped to temperature at 15°C/min and slowly cooled following the 3 h HIP period. The powders consolidated by extrusion were contained in low alloy steel cans and vacuum degassed at 400°C for 2 h. The sealed cans were then rapidly furnace heated to 850°C, thermally equilibrated, extruded through a die with a 7:1 reduction ratio and air-cooled.

2D. Characterization Techniques

In this work, characterization of the microstructural evolution, with emphasis on the NFs, was performed using various techniques, including: atom probe tomography (APT), small angle neutron scattering (SANS) and microhardness measurements. Selected combinations of these techniques were used to assess the effects of alloy composition, mechanical alloying (milling) parameters and consolidation conditions.

Small Angle Neutron Scattering

Small angle neutron scattering (SANS) was used to characterize the NFs. SANS is particularly useful in this case since the nm-scale features scatter neutrons at high angles (q values - see below), in a region that is otherwise dominated by low intensity uniform incoherent scattering [46]. The measurements were carried out on the 8 m SANS instrument (NG1) at the National Institute of Standards and Technology at an average neutron wavelength of λ = 0.5 nm. As illustrated in Figure1 a strong ≈ 1.7 tesla magnetic field applied in the horizontal direction permitted measurement of both nuclear, $d\Sigma/d\Omega(q)_n$, and magnetic, $d\Sigma/d\Omega(q)_m$, neutron scattering cross sections, where the total scattering cross section $d\Sigma/d\Omega\ (q,\phi)$ is

$$\frac{d\Sigma}{d\Omega}(q,\phi) = \frac{d\Sigma}{d\Omega}(q)_n + \sin^2\phi \frac{d\Sigma}{d\Omega}(q)_m \qquad (1)$$

Here, ϕ is the angle with respect to the magnetic field direction and q is scattering vector that is related to λ and the scattering angle, 2θ, as

$$q = 4\pi\sin\theta/\lambda \qquad (2)$$

The number of neutrons scattered at q and ϕ were measured with a 64 by 64 cm position sensitive ^{3}He detector with a pixel size of ≈ 5 mm. By locating the detector 2 m from the specimen and rotating it ≈ 5° off the beam axis, the maximum q was ≈ 3 nm^{-1} for ϕ from 0 to 45°; the maximum q decreased to ≈ 2 nm^{-1} at ϕ = 90°.

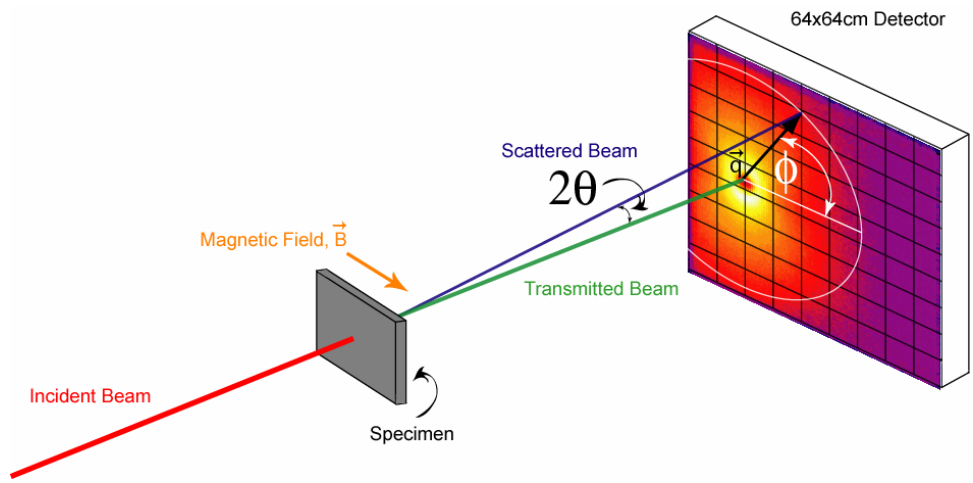

Figure 1 Experimental configuration used in the SANS measurements showing the incident beam and specimen in an applied magnetic field producing a 2D scattering pattern on the position sensitive detector.

The $d\Sigma/d\Omega(q,\phi)$ were determined as follows. The detector counts at a pixel location associated with measurements of background radiation and counts from parasitic neutron scattering were subtracted from the measured total, thus giving the number of neutron counts associated with the sample itself, $I_s(q, \phi)$. The corresponding $I_w(q, \phi)$ for a water standard, with a known $d\Sigma/d\Omega(q,\phi)_w$, was also measured. The calibrated $d\Sigma/d\Omega(q,\phi)_s$ is given by

$$\frac{d\Sigma}{d\Omega}(q,\phi)_S = \frac{d\Sigma}{d\Omega}(q,\phi)_W \left[\frac{n_S}{n_W}\right]\left[\frac{t_S}{t_W}\right]\left[\frac{\phi t_S}{\phi t_W}\right]\left[\frac{I_S(q,\phi)}{I_W(q,\phi)}\right] \quad (3)$$

Here the n, t and ϕt are the number of atoms, the fraction of neutrons transmitted through the sample and the total fluence of neutrons, for the sample (S) and water standard (W), respectively.

The absolute cross-sections were averaged over specified detector q and ϕ ranges (typically, ϕ = 0±30, 45±15 and 80±10). The scattering cross sections for the nanometer features associated with the variable of interest, $d\Sigma/d\Omega(q,\phi)_f$, were determined by subtracting a corresponding control cross section, $d\Sigma/d\Omega(q,\phi)_c$. For example, as illustrated in Figure 2, subtracting the $d\Sigma/d\Omega(q,\phi)_c$ for 12WT from the $d\Sigma/d\Omega(q,\phi)_s$ for J12YWT was used to assess the effect of adding Y_2O_3 to an alloy containing W and Ti. The SANS data analysis based on other choices of controls resulted in generally similar conclusions [38].

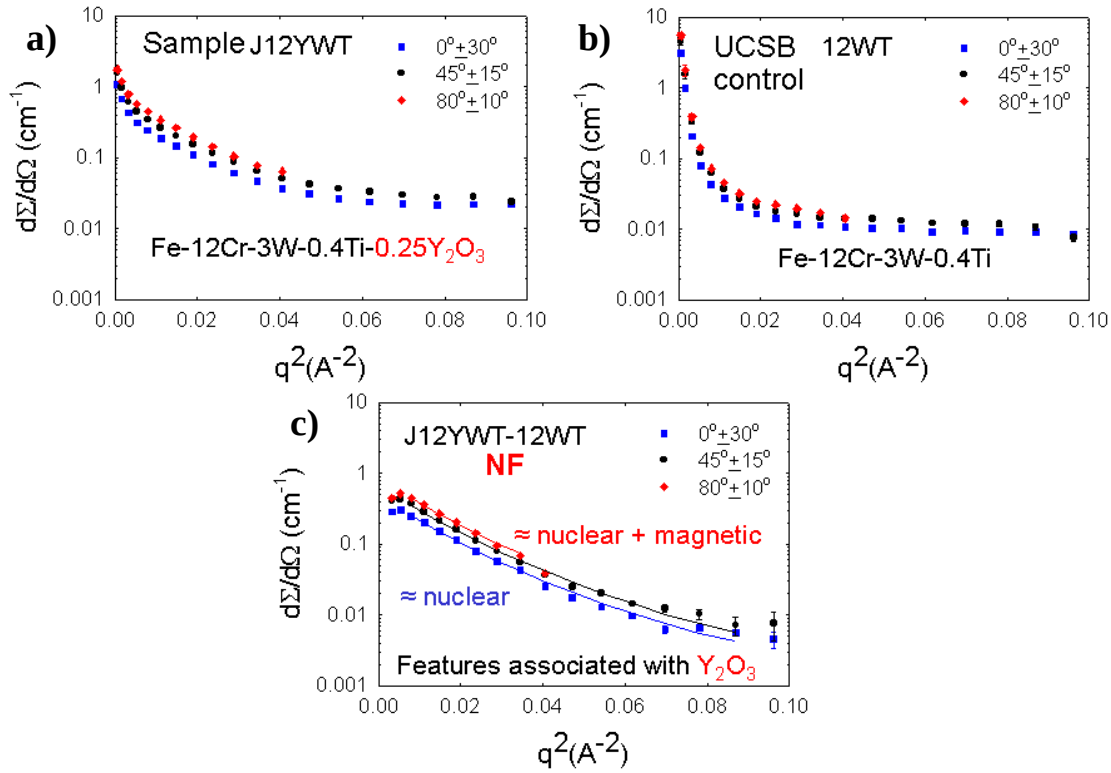

Figure 2. Illustration of the SANS data analysis procedure that subtracts control dΣ/dΩ data (U12WT1150) from that for specimen (J12YWT) to identify the scattering associated with NFs.

The $d\Sigma/d\Omega(q,\phi)_f$ is determined by the number density (N), radius (r), volume fraction (f), shape (taken as non-interacting spheres) and scattering length density (ρ) difference between the nm-scale features (ρ_f) and the matrix (ρ_m) they are embedded in, $\Delta\rho = \rho_f - \rho_m$, where $\Delta\rho$ is the scattering contrast factor. For specified features and specified size (r),

$$\frac{d\Sigma}{d\Omega}(q,\phi) = Nf^2(\Delta\rho)^2|S(qr)|^2 \tag{4}$$

Here, S(qr) is a small angle scattering form factor that depends on the feature shape [46]. The ρ_f and ρ_m, and $\Delta\rho$, differ for nuclear versus magnetic scattering. The nuclear scattering ρ^{nuc} depends on the compositions of the feature and the matrix and their average atomic volumes V, respectively, as

$$\rho^{nuc} = \sum_i \frac{b_i X_i}{V} \tag{5}$$

Here b_i is the isotope averaged scattering length for element i, X_i is the atom fraction of that element in the feature or matrix. Thus the matrix and scattering feature compositions and average atomic volumes must be known to determine $\Delta\rho^{nuc}$. The magnetic scattering length density ρ_f^{mag} was taken as 0 for the NFs composed of Ti, Y and O and the ρ_m^{mag} corresponded to the Fe-14Cr composition of the matrix. Thus even if the composition of the scattering feature is not known, the magnetic $\Delta\rho^{mag}$ can be specified with good precision. The assumption that $\rho_f^{mag} = 0$ was tested by measuring the variation of $d\Sigma/d\Omega(q)_{mag}$ with temperature. The observed decrease in $d\Sigma/d\Omega(q)_{mag}$ with increasing temperature could be entirely explained by the corresponding decrease in the saturation magnetization of the Fe-Cr-W matrix, consistent with the hypothesis that $\rho_f^{mag} = 0$.

The $d\Sigma/d\Omega(q)_{mag}$ was determined from the $d\Sigma/d\Omega(q,\phi)$ data for the entire detector based on a best fit for magnetic to nuclear scattering ratio, $M/N = [\Delta\rho^{mag}]^2/[\Delta\rho^{nuc}]^2$, as

$$\frac{d\Sigma}{d\Omega}(q)_{mag} = \frac{d\Sigma}{d\Omega}(q,\phi)\Big/\left[N/M + \sin^2(\phi)\right] \tag{6}$$

Alternatively, the $d\Sigma/d\Omega(\phi)$ data was q and ϕ averaged over a large q range (typically, 0.8 - 1.8 nm^{-1}) for 8 to 10 average $\sin(\phi)^2$ values from ≈ 0 to 1. The average $d\Sigma/d\Omega(\phi)$ were then least squares fit to determine the M/N as

$$\frac{d\Sigma}{d\Omega}(\phi) = \frac{d\Sigma}{d\Omega_{nuc}}\left[1 + \frac{M}{N}\sin^2(\phi)\right] \tag{7}$$

Here, $d\Sigma/d\Omega_{nuc}$ and M/N are the best-fit parameters.

Of course the nm-scale features have a distribution of sizes, r. In this analysis, the distribution was described by a lognormal function, as parameterized by a mode radius, r_m, and a distribution width parameter β [38, 47]. The r_m and β were found by least square fitting Equation 4, modified to account for the lognormal size distribution, to the reduced $d\Sigma/d\Omega(q)_{mag}$ data. Note, the lognormal is used for convenience and due to the fact that it does not admit negative values of r, and the degree to which it is an approximation of the actual distribution is believed to have negligible effects on the results, especially when compared to other sources of uncertainty. The r_m and β are related to the average nm-scale feature r, <r> (actually $\langle r\rangle = \{\langle r^3\rangle\}^{1/3}$) as

$$r = \langle r \rangle = r_m \exp\left(\frac{3\beta^2}{4}\right) \tag{8}$$

Note that r depends on the shape, but not magnitude of $d\Sigma/d\Omega(q)_{mag}$. The corresponding nm-scale feature N and f scale with $d\Sigma/d\Omega(q)_{mag}$ and are given by

$$N = \left(\frac{3}{4\pi}\right)^2 \left[\frac{\exp\left(-9\beta^2\right)}{r_m^6 \rho_{mag}^2}\right] \frac{d\Sigma}{d\Omega}_{mag}(0) \tag{9}$$

$$f = \left(\frac{3}{4\pi}\right) \left[\frac{\exp\left(-6.75\beta^2\right)}{r_m^3 \rho_{mag}^2}\right] \frac{d\Sigma}{d\Omega}_{mag}(0) \tag{10}$$

Here, $d\Sigma/d\Omega_{mag}(0)$ is the magnetic scattering at q = 0. Note different combinations of r_m and β can give nearly equivalent fits to the $d\Sigma/d\Omega(q)_{mag}$ data. This covariance has little effect on f and only a modest effect on r, but this has a significantly larger effect on N.

The analysis described above is applicable when there is only one type of scattering feature. However, in some cases it is not possible to fit the $d\Sigma/d\Omega(q)_{mag}$ with a single lognormal distribution, which indicates the presence of multiple scattering features. The presence of multiple features with different sizes is also suggested by a significant q-dependence of the M/N ratio. In such cases, the fitting can be carried out for two features with different r_m, β and M/N parameters.

SANS was also performed on unconsolidated powders. Precisely weighed quantities of milled powders were loaded in pure 1100 Al capsules with thin windows that were sealed with an O-ring in a dry-Ar glove box. The neutron beam was masked to be slightly larger than the capsule powder pocket and slightly smaller than the O-ring diameter. Empty container runs were used to characterize the parasitic scattering from the Al capsules. In the data reported here, the annealed powder data had the same time-temperature history as the HIPed alloys.

The results of the SANS measurements are described below. More detailed description of the SANS data collection, reduction and analysis procedures can be found in Reference 38 and 47.

Microhardness
Diamond pyramid Vickers microhardness measurements (kg/mm^2) were performed with a LECO M-400A semi-automated testing instrument. The microhardness values for the consolidated alloys with 0.05 μm diamond surface finish, at a 1000 g load, were based on the average of a minimum of five indents. Microhardness measurements were also performed on milled powders mounted in bakelite and flat polished to a 0.05 μm diamond finish. Individual indents were made on the particles that were on the larger end of the powder size distribution. However, the actual dimensions of the mounted, flake shaped powders were not known, and some were rather thin. Thus the load for powder indentations was reduced to 50 g. The powder microhardness measurements that were anomalously low were eliminated, since this is an indication that the particle was too thin to provide an accurate measurement.

Atom Probe Tomography
Atom probe tomography (APT) specimens were prepared by standard electropolishing methods [48]. The APT characterizations was performed at the Oak Ridge National Laboratory (ORNL), with the assistance of Dr. Mike Miller, on the Imago local electrode atom probe (LEAP), as part of the SHaRE program. The measurements were performed at a specimen temperature of 50–60 K, pulse repetition rate of 100 kHz, and a pulse fraction of 20% of the standing voltage. The atom maps were analyzed using Imago and ORNL's in-house software. All NF compositions quoted in this paper are atom fractions.

RESULTS

The results section is divided into three sections. The first describes the characterization of the as-milled powders to determine the key mechanisms occurring during this stage of processing. The second section describes the effects of milling, thermal history and compositional variables on the NFs in consolidated alloys. The NFs formed in base alloy powders annealed with the same time temperature history as the HIP cycle are also compared to the consolidated alloys. The final section describes what is known about the character of the NFs.

Characterization of the As-milled Powders
The hardness of several as-milled powders (designated by a P, such as U14YWTP) are shown in Figure 3 along with that for the unmilled 14Cr powders. The error bars represent one standard deviation measures of the data scatter. The severe deformation imparted by mechanical alloying results in high hardness for both milling techniques and all alloy compositions. The high strength is associated with both small crystallite sizes (e.g., ≈ 20 to 24 nm in U14YTP and U14YWTP, respectively) and high lattice strains (e.g., 0.48 to 0.64% in 14YTP and P14YWTP, respectively) as measured with X-ray diffraction (XRD) methods [38,49]. The SPEX milled powders were ≈ 20% harder than the attritor milled powders, consistent with the higher energy of former milling method that leads to the larger lattice strains and smaller crystallite sizes [38]. The addition of Ti to U14YP (U14YTP) powders results in a small increase in hardness but there is little additional effect of the addition of W (U14YWTP). Notably the SPEX milled powders containing both Y and Ti reach remarkable hardness levels of ≈ 1000 kg/mm^2, which is roughly equivalent to a uniaxial flow stress of 3000 MPa.

No oxides were observed in the as-milled powders by XRD [38]. This is consistent with the SANS data in Figure 4, showing $d\Sigma/d\Omega$ versus q^2 plots at 45° to the applied magnetic field. The 45° curves are presented because they have the highest q range, and include both the nuclear and about 50% of the magnetic scattering contributions. Scattering curves for the unmilled 14WT and the U14YWT alloy HIPed at 850°C are compared to those for the various as-milled powders. Figure 4a shows 45° scattering curves for milled U14YWTP (filled circles), O14YWTP (filled diamonds) and U14WTP (filled triangles) powders. Figure 4b shows the corresponding as-milled powder scattering curves for U14YTP (filled squares), U14Y(M)TP (filled inverted triangle), U14YP (filled right triangle), U14WTP (filled triangles). The scattering curves for all the as-milled powders are similar, and are somewhat higher than those for the un-milled U14WT (open triangles) and U14 powders (not shown). The milling induced scattering may be due to solutes, including O introduced during milling and very small sub-nm solute clusters, as well as contributions from the high dislocation density and small grain sizes. The increase in scattering at lower q

in the U14YTP may indicate the presence of low number density of larger scattering features, perhaps as the result of incomplete dissolution of Y_2O_3, incorporation of Cr_2O_3 oxide scales during milling, or additional oxidation of the powders prior to SANS. Note some of the differences in the magnitudes of the as-milled scattering curves may also be due to uncertainties in the mass of the powder actually probed by the neutron beam.

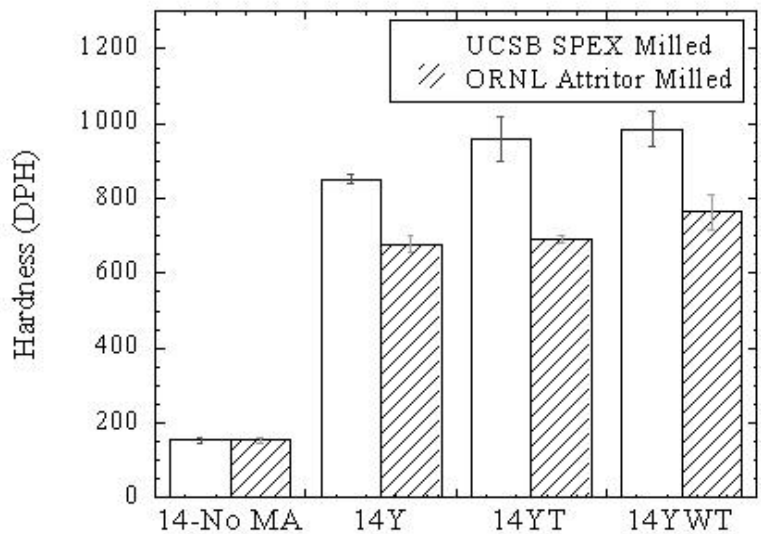

Figure 3. Hardness of the SPEX and attritor as-milled powders showing the effects of the additions of Y, Ti and Y, Ti, W.

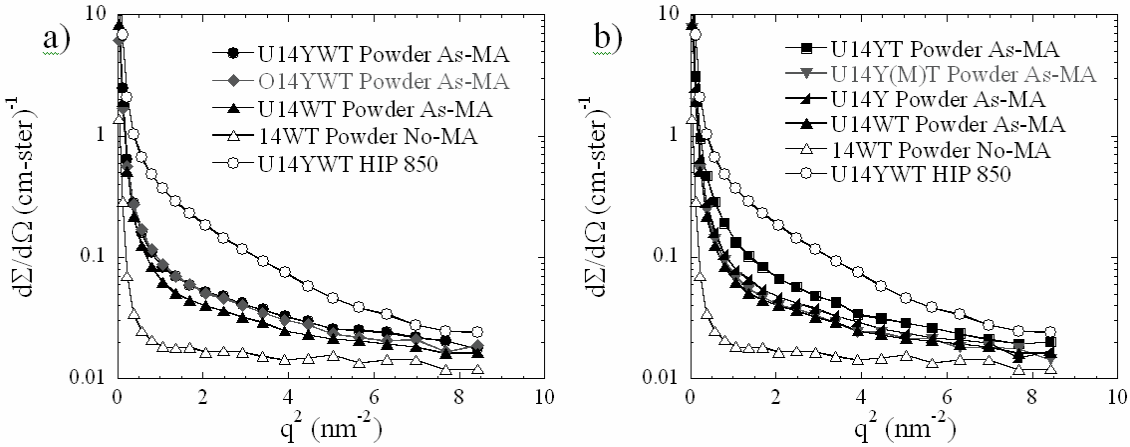

Figure 4. SANS scattering curves at 45° for unmilled 14WT powders and the U14YWT alloy HIPed at 850°C compared to the corresponding scattering curves for the various as-milled powders.

Irrespective of the small differences, however, analysis of these results show the extra scattering at higher q after milling is from very small features with sizes equivalent to radii of ≈ 0.5 nm or less. In stark contrast, the scattering curve for the U14YWT HIPed at 850°C (unfilled circles) shows a high number density of nm-scale precipitates formed during hot consolidation, as indicated by the large bulge in the $d\Sigma/d\Omega$ curve between $q^2 \approx 1$ and 6 nm^{-2}. Thus the SANS data suggest that most of the Y, Ti and O are dissolved into the Fe-14Cr alloy matrix during both SPEX and attritor ball milling, forming highly

supersaturated solid solutions, along with some very small sub nm solute clusters or Y-O and/or Ti-O complexes. The major corollary conclusion from the milling study is that the NFs form during hot consolidation and or powder annealing. The detailed kinetics of precipitation will be discussed in detail in a future publication.

The effect of annealing on the hardness of the powders is shown in Figure 5 for 1 h anneals in 75°C increments between 850 and 1150°C for the SPEX milled powders and in 150°C increments for the attritor milled powders. Annealing involved increasing the temperature at a rate of 15°C/min (equivalent to the HIP ramp), holding at the designated temperature for 1 h, and air-cooling. The Figure 5a shows that the SPEX milled U14P hardness recovers completely after annealing at 850°C. The recovery in the U14YTP and U14YWTP powders increases with increasing annealing temperature. However, the residual hardening in the powders with both with Y and Ti is still significant after the 1150°C anneal. Both the pre and post milling hardness is lower in the U14YWP powder, with Y but not Ti. Figure 5b shows the corresponding results for the attritor milled powders. The general annealing trends are similar, but the overall hardness is lower in the attritor milled powders.

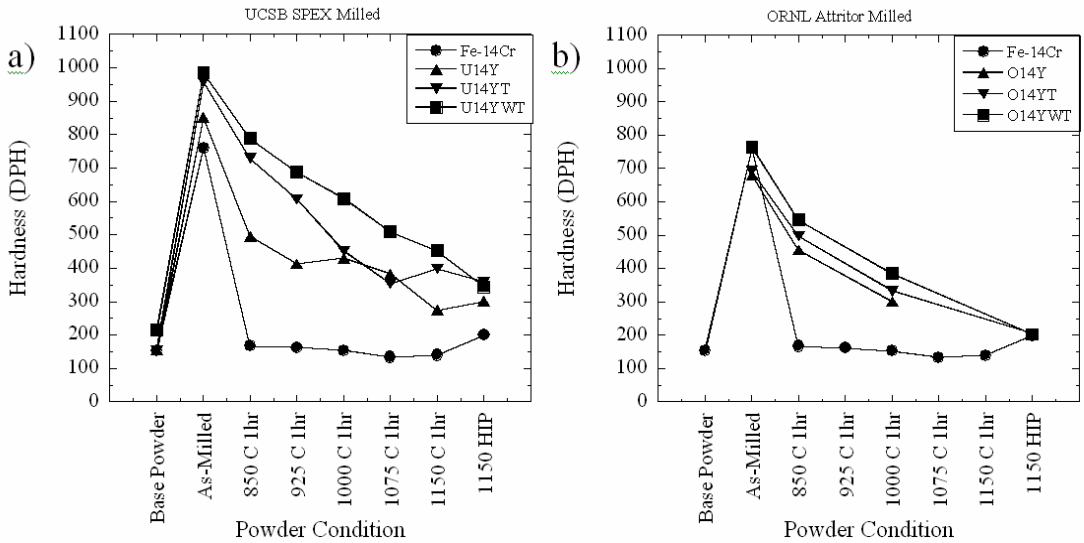

Figure 5. Hardness as a function of 1 h annealing at temperature from 850 to 1150°C for: a) SPEX and b) attritor milled powders.

The effect of 1150°C HIPing of un-milled versus SPEX milled 14Cr powders on SANS 45° scattering curves is shown in Figure 6. The scattering at low q is increased slightly by the milling. Again, this is probably due to oxidation and impurity pickup during milling, possibly leading to a limited amount of internal Cr oxidation, or incorporation of oxide layers in the milled powders.

Powder Consolidation

The consolidation path has a very important influence on the as-processed microstructure. The most obvious difference between the two consolidation techniques used in this study is that hot extrusion produces anisotropic elongated and textured grains, while HIPing produces more equiaxed microstructures. However, there are also variations in the time-temperature history and mechanical deformation that may also influence the NFs, as well as the dislocation and grain structures in the two cases, even at the same nominal consolidation temperature. Thus, the effects of the two milling and two consolidation methods were compared for MA 14YWT. In addition to the UCSB and ORNL model alloys, two NFAs produced by commercial vendors, INCO MA957 and Kobe Steel J12YWT, were also characterized.

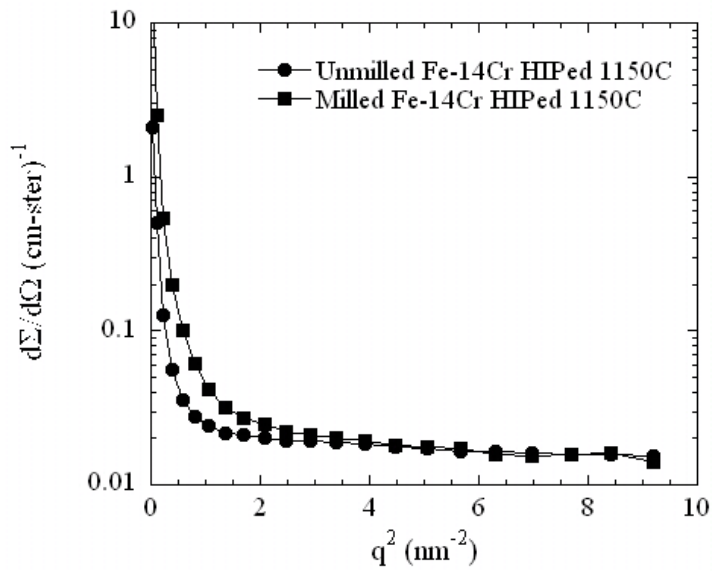

Figure 6. SANS 45° scattering curves showing the small effect of milling on the 45° scattering curves for U14(Cr) alloys HIPed at 1150°C.

Figure 7 shows the effect of HIP consolidation temperature on the nm-scale precipitates in the baseline model alloy, U14YWT, including the NF size (r), number density (N), volume fraction (f), as well as the alloy microhardness (H). As expected, the NF N and f decrease, while the corresponding r increases, with increasing HIPing temperature. The NF parameter ranges for HIPing at 850 to 1150°C were r ≈ 1.2 to 1.7 nm, f ≈ 2.2 to 0.6% and N ≈ 2.6 to 0.3x10^{24} /m^3. In the case of the alloy HIPed at 1150°C, it was necessary to fit r, f, N and M/N parameters for both a small NFs (r ≈ 1.7 nm) and a much larger, nominally an oxide type feature, with r ≈ 11.4 nm. Because the larger features are near the limits of resolution for the SANS configuration used in this study, they are not discussed further; hence, our primary focus is on the NFs. Note, the larger precipitates, that were also observed for several other alloy conditions, are better characterized by TEM [19]. Figure 7 also shows that the hardness of U14YWT decreases from 635 to 344 kg/mm^2 with increasing HIPing temperature from 850 to 1150°C

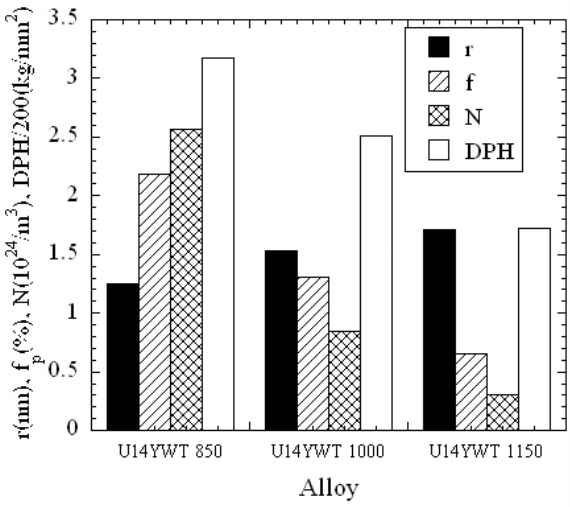

Figure 7. SANS r, f, N and H data showing the effect of HIP consolidation temperatures of 850, 1000 and 1150°C on the UCSB base alloy U14YWT.

Figure 8 compares the r, f and N of the NFs in the HIPed U14YWT with those that form in annealed U14YWTP powders subject to the same ramped time temperature history. Clearly, the NFs are similar in the two cases, indicating that the deformation that occurs during HIPing has little effect on the Y-Ti-O clustering-precipitation process.

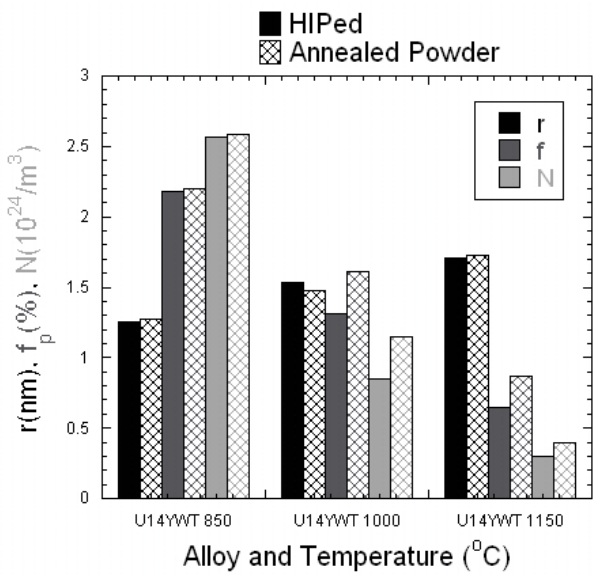

Figure 8. SANS r, f, N and H data showing that the NFs formed in HIPed alloys and annealed powders are very similar.

Figure 9 shows a 3-dimensional APT map for U14YWT HIPed at 1150°C with a grain boundary at the center of the map that is slightly enriched in Cr and W, as shown in Figure 9b and c, along with trace amounts of impurity C and N as shown in Figure 9d and e. However, there is no evidence of carbide/nitride formation, or of the presence of any other second phases, like Fe_2W-Laves, Cr rich α' or σ-phases, or $Fe_{17}Y_2$. Further, there was no evidence of the presence of dissolved, or finely precipitated, Ar milling gas in the APT data. As shown in Figure 9f to j, the Y, Ti and O do not segregate to the grain boundaries; instead, these elements either remain dissolved, or are associated with the NFs. Figure10 shows the average composition of the NFs in U14YWT HIPed at 1000°C is ≈ 0.17 Y, 0.28 Ti, 0.33 O and 0.22 Fe, Cr and W. The composition of the NFs found in U14YWT HIPed at 1000 and 1150°C is very similar in to those previously observed by Miller in both MA957 and J12YWT [33-35]. However, unlike the commercial vendor alloys, the NFs in U14YWT and other model alloys were not homogeneously distributed. The heterogeneous distributions of NFs found in this study are similar to those found in other model alloys analyzed by Miller [36]. Section 3D provides a more detailed discussion of the composition and character of the NFs.

The SANS results for attritor milled O14YWT powders, both HIPed and hot extruded at 850°C, are shown in Figure 11. The hot extruded alloy has a somewhat larger NF f and N compared to the HIPed alloy. However, the latter is slightly harder. Hot extrusion results in more deformation than HIPing, and produces texture and grains that are elongated in the extrusion direction. As shown in Figure 12, the SPEX milled powders HIPed at 850 and 1000°C contain a higher N and f of similarly sized (r) NFs compared to the attritor milled alloys. However, no NFs are observed in the attritor milled alloy HIPed at 1150°C. In contrast, the SPEX milled alloy HIPed at 1150°C contains NFs (as well as some coarser oxides), but with lower f and N and larger r than for HIPing at lower temperatures. It should be noted these differences are not intrinsic to the mechanical alloying method, since, subsequent to these measurements, NFs were observed in more recent batches of attritor milled powders HIPed at 1150°C.

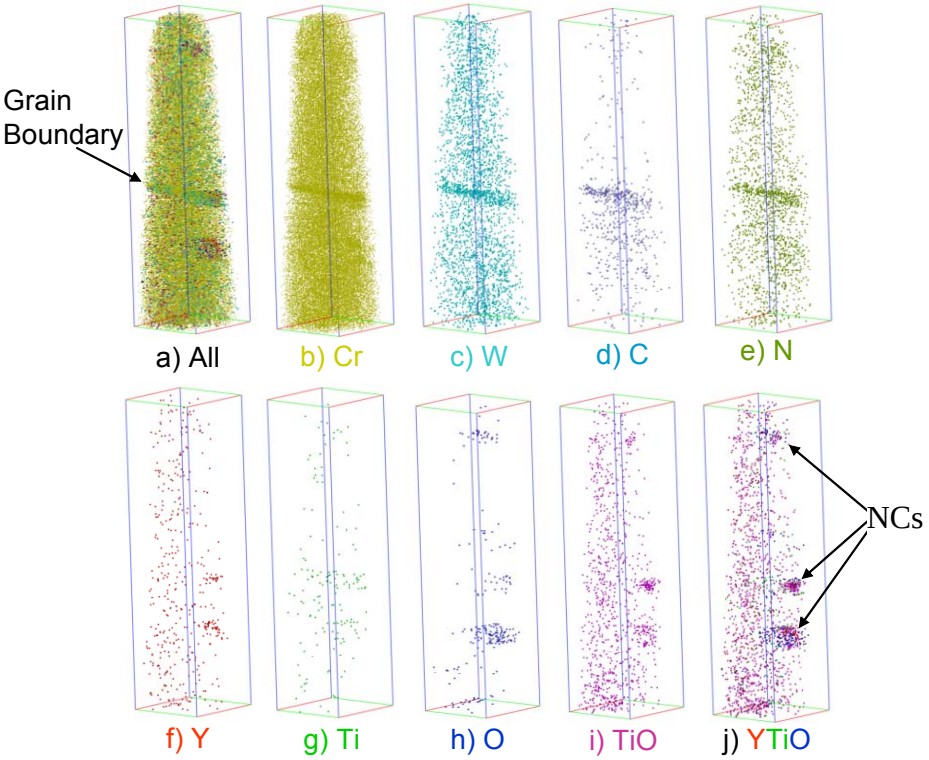

Figure 9. Atom probe tomography (APT) atom maps for U14YWT1150.

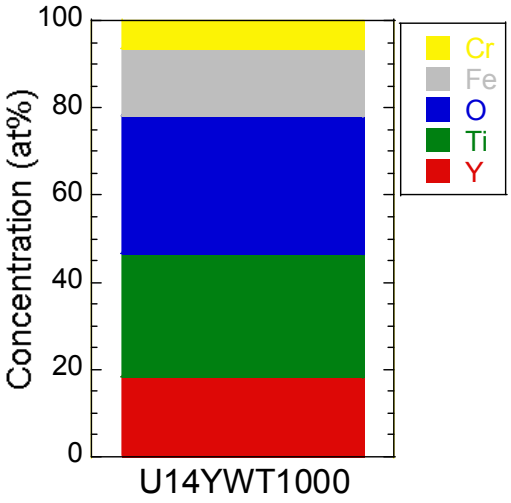

Figure 10. The average precipitate composition in U14YWT HIPed at 1000°C as determined by APT.

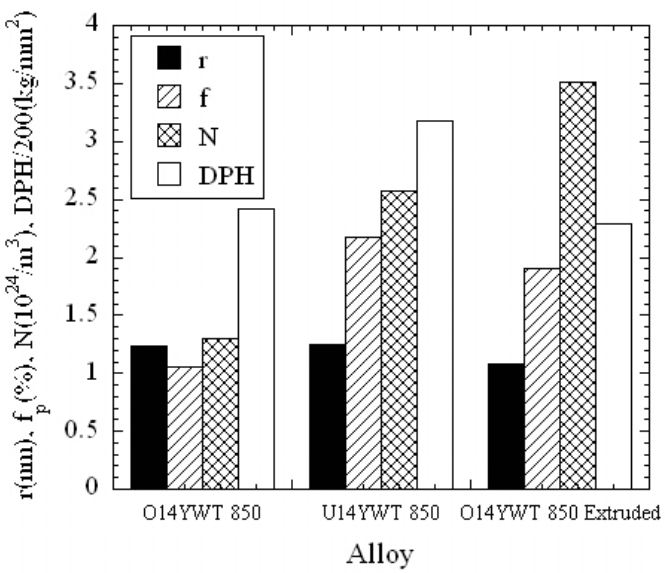

Figure 11. SANS r, f, N and H data showing the effect of HIP versus hot extrusion consolidation at 850°C for O14YWT. The results for U14YWT are also shown for comparison.

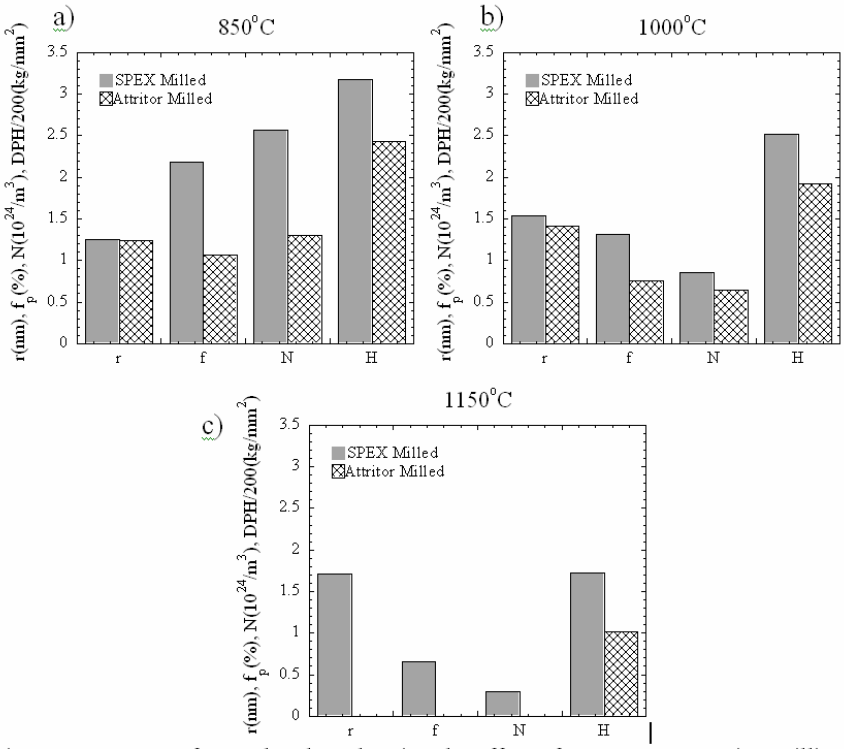

Figure 12. SANS r, f, N and H data showing the effect of SPEX versus attritor milling at a) 850, b) 1000, and c) 1150°C.

The critical effects of alloy composition in SPEX milled alloys are shown in Figure 13a for HIPing at 850°C and in Figure 13b for HIPing at 1150°C. All the alloys contain Y. Two other alloys add either W or Ti and a third contains both W and Ti. In the case of HIPing at 850°C, all of the alloys contain NFs with similar r, but with f and N that increase somewhat with the addition of Ti. The hardness is also significantly higher

in the alloys with Ti, and is also larger in the alloys with W, especially the one with Y and Ti. In the case of HIPing at 1150°C, NFs do not form in alloys without Ti. Rather, the Y-bearing alloys without Ti, contain a significant volume fraction of much larger features. Increase in hardness with the addition of Ti of the alloys HIPed at 1150°C is less than for HIPing at 850°C, and adding W appears to lead to a small degree of softening in this case. These results are generally consistent with previous TEM and APT results reported by showing a larger number of smaller NFs in Ti bearing alloys processed at 1150°C [2,19, 33]. As discussed elsewhere the relationship of N, r and f to the alloy hardness is consistent with accepted models of dispersed barrier strengthening [38]. Thus, both Y and Ti are necessary for the formation of NFs at higher consolidation temperatures.

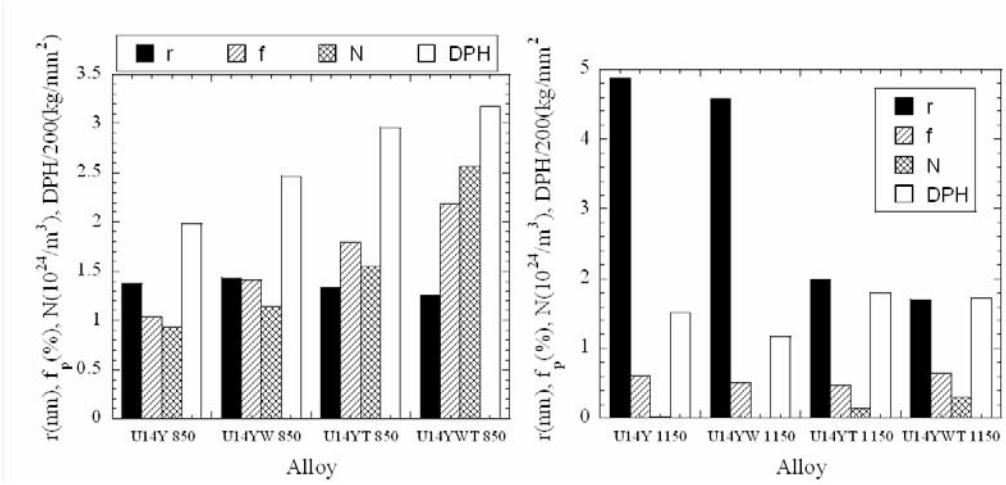

Figure 13. SANS r, f, N and H data showing the effect of alloy chemistry for alloys HIPed at 850°C (a) and 1150°C (b).

Figure 14 shows the effect of SPEX milling U14T powders with metallic Y (U14Y(M)T) versus Y_2O_3 oxide powders (U14YT) followed by HIPing at 850°C. The similarity of the r, N and f in the two cases indicates that the intentional addition of oxygen is not essential to the formation of the NFs, at least at this lower consolidation temperature. This is likely due to oxygen pick-up during MA.

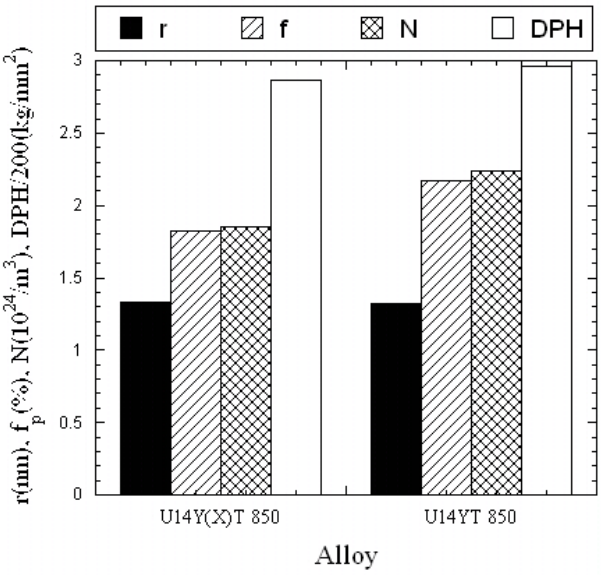

Figure 14. SANS r, f, N and H data showing the minimal effect of milling with yttrium metal (Y) versus yttria (Y_2O_3) on r, N, f.

Figure 15 compares the NFs in U14YWT HIPed at 1150°C to those found in commercial vendor alloys MA957, J12YWT (reported to be hot extruded at 1150°C). SANS controls for these NFAs were fabricated by SPEX milling and 1150°C HIP consolidation of Y-free powders with otherwise similar compositions to the vendor alloys. Note SANS measurements were also carried out for PM2000 but NFs were not found in this case (not shown). However, the r, f and N in the UCSB base model alloy U14YWT are similar to those in MA957 and J12YWT.

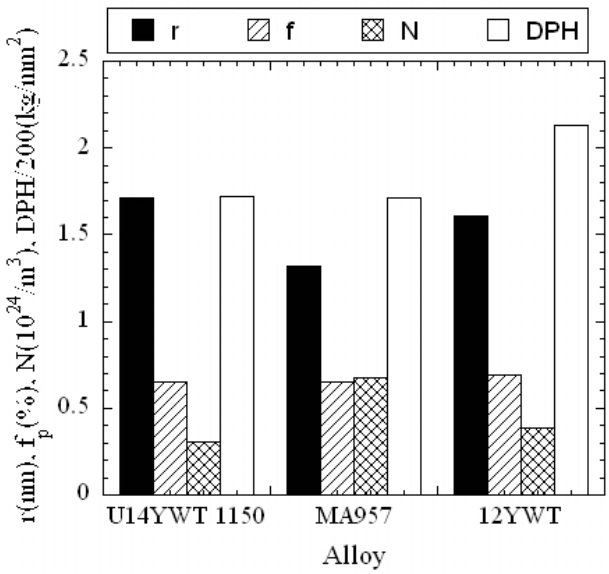

Figure 15. SANS r, f, N and H data comparing U14YWT1150, MA957 and 12YWT.

The SANS results on J12WYT can be compared to APT data on the same alloy reported by Miller [33,35]. The nominal average APT radius is slightly larger than the corresponding r from SANS and the NF number density is substantially higher than the N from SANS. However, the small differences in the radius are likely due to the local APT magnification effect, and the APT technique samples a much smaller volume of material than SANS, hence, may not account for spatial fluctuations in the NF number densities. Miller reports that he typically uses data from the regions that are richest in the features being probed [50]. Indeed, using the nominal radius and local number density from the APT data would produce a nominal volume fraction of NFs that is far too high to be physical. Thus, the overall agreement between the two techniques is reasonable.

However, there is one significant difference between the HIPed model and the commercial vendor alloys that is not shown in Figure 15. That is, the magnetic to nuclear scattering ratios (M/N) are ≈ 1.2 for MA957 and 0.9 for J12YWT, are much lower than the M/N > 2 for U14YWT. The significance of this observation is briefly discussed in Section 3D below, and will be addressed in more detail in future publications.

The results in Sections 3A and 3B can be summarized as follows:

1. MA dissolves Y and O in the Fe alloy powder matrix.

2. The dissolved Y, O and, when present Ti, precipitate during hot consolidation in the form of NFs and larger oxide phases, depending on the alloy composition and processing time-temperature history.

3. The NF f and N decrease and their size (r) increases with increasing HIPing temperature.

4. Hot extrusion versus HIPing at 850°C has a modest effect on the NFs.

5. NFs form in alloys containing Y and Y plus Ti HIPed at 850 and 1000°C.

6. Ti is necessary to form NFs during HIPing at 1150°C.

7. NFs form in SPEX milled, but not attritor milled, alloys containing Y and Ti during HIPing at 1150°C; however, this is not the case for more recent batches of attritor milled powders, also HIPed at 1150°C.

8. Milling with metallic Y produces similar NFs in powders milled with Y_2O_3 during HIPing at 850°C.

9. The NF f, N and r in the baseline U14YWT alloy HIPed at 1150°C are similar to those in the commercial vendor MA957 and JY12YWT alloys that were hot extruded at the same temperature.

The microhardness data on the various alloys in the preceding sections is of direct interest as a metric of strength, and also reflects the underlying micro/nano-structural variations. Figure 16 summarizes the microhardness data trends for various alloys and processing conditions. The addition of Ti or W alone, or in combination, does not have a large systematic effect on hardness. The addition of Y does increase hardness, but the alloys with the highest hardness contain both Ti and Y. There is also a systematic effect of higher hardness for SPEX milled powder alloys compared to those consolidated from attritor milled powders. Finally, as expected, the hardness in alloys with Y and Y plus Ti, decreases with increasing consolidation temperature. These observations are consistent with the conclusion that, while they are not the only source of hardening relative to the control alloys, NFs are necessary for significant strengthening, at least low test temperatures. The quantitative relation between the NFs and microhardness will be presented in a future publication.

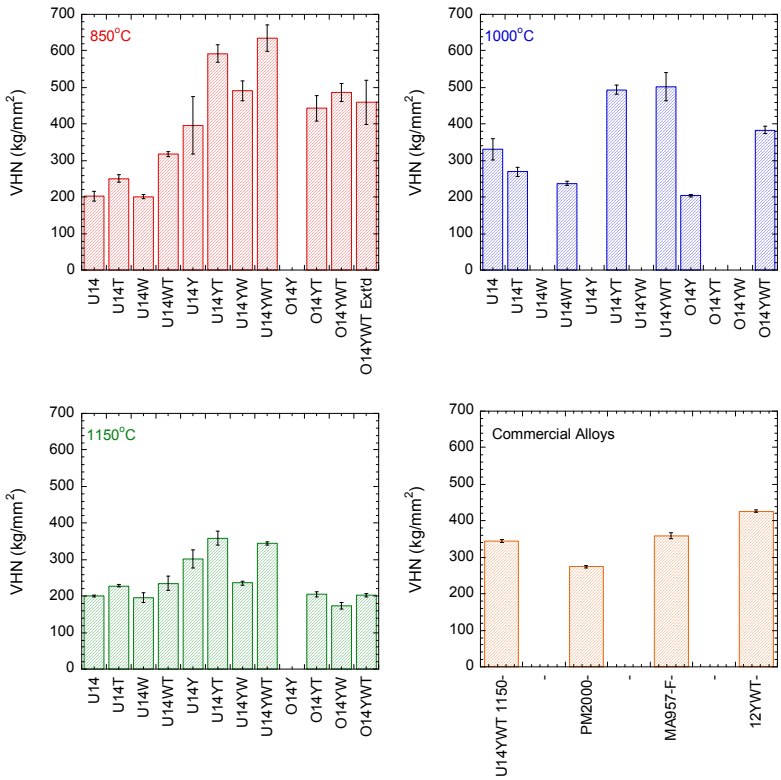

Figure 16. Summary of the hardness trends for a) alloys consolidated at 850°C, b) 1000°C, c) 1150°C and d) commercial vendor alloys.

The Composition and Character of the NFs

The results of the systematic SANS measurements show that the NF form by clustering and precipitation of Ti, Y and O from solid solution. As expected, the number densities and volume fractions of the NFs decrease and their radii increase with higher HIPing temperatures. However, we have not yet addressed the nature of the NFs. Information on the composition of the NFs is contained in the SANS magnetic to nuclear scattering ratio, M/N, which is given by

$$M/N = (\rho_f^{nuc} - \rho_m^{nuc})^2/(\Delta\rho_m^{mag})^2 \quad (11a)$$

$$\rho_f^{nuc} = \Sigma_i X_{if} b_i^{nuc}/V_f \quad (11b)$$

$$\rho_m^{nuc} = \Sigma_i X_{im} b_i^{nuc}/V_m \quad (11c)$$

$$\rho_m^{mag} = b_m^{mag}/V_m \quad (11d)$$

Here, the ρ^{nuc} are the average nuclear scattering length densities, the b_i^{nuc} are the isotope averaged nuclear scattering length of the element i, the X_i are the atom fractions of element i, the V are the average atomic volumes in the NFs (f) and matrix (m), respectively. The ρ_m^{mag} is the magnetic scattering length density of the Fe-14Cr-3W matrix, which was taken as 0.82 times that for unalloyed Fe at 23°C. Thus, the M/N depends on the composition of the NFs.

The nominal M/N for the common complex Y-Ti oxides are shown in Table 2, along with the measured values for NFs in U14YWT and the commercial vendor alloys J12YWT and MA957. The corresponding maximum volume fractions of the oxides, f_{max}, are limited by mass balances, and can be estimated assuming all the Y is precipitated as

$$f_{max} = X_{yf}(V_f/V_m) \quad (12)$$

The f_{max} for the common complex oxides are also show in Table 2 along with the measured values.

Table 2 Computed and Measured NF M/N Ratios and Volume Fractions or Maximum Computed Volume Fractions

Oxide/Alloy	M/N	f or f_{max} (%)
Y_2TiO_5	1.60	0.57
$YTiO_3$	2.14	0.61
$Y_2Ti_2O_7$	1.04	0.87
U14YWT-850	2.50	2.18
U14YWT-1000	2.30	1.31
U14YWT-1150	2.10	0.65
J12WYT	0.90	0.69
MA957	1.20	0.65

The SANS data for both the J12YWT and MA957 are reasonably consistent with a $Y_2Ti_2O_7$ pyrochlore complex oxide phase. The corresponding SANS data for U14YWT HIPed at 1150°C is consistent with the $YTiO_3$ complex oxide. However, the volume fractions of the U14YWT alloys HIPed at 850 and 1000°C are too high to be explained by the presence of these oxide phases alone, and the M/N are somewhat higher than for the oxides shown in Table 2, especially at 850°C. The combination of high f and M/N suggest that the NFs may contain Fe.

Note, that the high f and M/N in the HIPed versus the extruded alloys are associated with differences in the temperature cycle experienced in powder consolidation in the two cases. In the case of HIPing, the powders were slowly heated to the consolidation temperature over a period of about 1 h, thereby allowing precipitation to occur at lower temperatures. In contrast the MA957 and J12YWT extrusions were rapidly heated to 1150°C, thus they experience less low temperature precipitation. This conclusion was confirmed by SANS studies of powders that were heat-treated both with ramp anneals that simulated the HIP cycle, and fast anneals that were closer to the temperature cycle experienced by the extruded alloys. The f = 0.44% and M/N = 0.94 for fast annealing of the U14YWTP powder at 1100°C are consistent with SANS data for J12YWT. The results of the powder annealing T-t precipitation kinetics study will be reported elsewhere.

The amount of Fe that rationalizes the high M/N and f_{max} can be estimated assuming a nominal value for V_f/V_m, that all the Y is in the NFs with a specified metal to oxygen atom ratio, M/O. Taking V_f/V_m = 1 and M/O = 2.5 (typical of that found in APT - see below) yields Fe contents of 0.36, 0.31 and 0.25 for U14YWT HIPed at 850, 1000 and 1150°C, respectively. The corresponding fractions of Y are 0.06, 0.1 and 0.16, resulting in Ti/Y ratios of 3, 1.9 and 1.25 at 850, 1000 and 1150°C, respectively. Of course other compositions derive from different assumptions about V_f/V_m and M/O.

In principle, the NF compositions can be precisely measured by APT. A fractional composition of ≈ 0.18 Y, 0.27 Ti, 0.33 O and 0.22 Fe and Cr was observed in the U14WYT HIPed at 1000°C. Note, the metal to oxygen atom ratio (M/O) of ≈ 2 and the Y plus Ti solute (S) to oxygen atom ratio (S/O) of ≈ 1.36 are inconsistent with any known oxide phase. Assuming V_f/V_m = 1, the maximum volume fraction for this composition is f_{max} = 0.69%. This is less than measured by SANS (1.31%). The corresponding calculated M/N ratio is ≈ 1.34 is also much less that the measured value of 2.3.

Miller et al have carried out APT measurements on MA957 and J12YWT that were extruded at 1150°C [33-36], as well as a MA Fe-14Cr-3W-0.4Ti-0.25Y_20_3 (O14YWT) extruded at 850°C [35]. The fractional compositions of the NFs in these alloys are summarized in Table 3. The calculated M/O, S/O, Ti/Y from the APT measurements are summarized in Table 4, which also shows the corresponding M/N and f_{max} assuming V_f/V_m = 1 and that f_{max} is limited by the total amount of Y, and the cases for NF with very low Y content, Ti as well.

Table 3 Summary of NF Fractional Compositions Derived From APT

Alloy	Y	Ti	O	Fe + Cr	Ref
U14YWT*	0.17	0.28	0.33	0.22	this work
MA957	0.15	0.33	0.40	0.12	xx
J12YWT	0.09	0.20	0.24	0.47	xx
J12YWT	0.08	0.42	0.40	0.10	xx
J12YWT	0.06	0.39	0.42	0.13	xx
O14YWT**	0.06	0.42	0.46	0.06	xx
Aver.	0.10	0.34	0.37	0.19	-
Aver. W/o Fe	0.13	0.42	0.45	-	-

* HIPed at 1000°C; ** Extruded at 850°C

Table 4 Calculated M/N Based on APT Compositions, Metal to Oxygen, Solute to Oxygen, Titanium to Yttrium Ratios and Measured and Estimated Maximum Volume Fractions

Alloy	M/O	S/O	Ti/Y	M/N	f_c
U14YWT*	2.00	1.36	1.50	1.34	0.69
MA957	1.50	1.21	2.20	0.87	0.81
J12YWT	3.17	1.21	2.20	2.30	1.25
J12YWT	1.24	1.14	5.25	0.55	1.20
J12YWT	1.38	1.07	6.50	0.53	1.20
O14YWT**	2.17	2.00	6.70	0.56	1.20

* HIPed at 1000°C; ** Extruded at 850°C

Taken at face value, the APT M/O and S/O ratios suggest that the NFs are not a known complex oxide phase. The APT composition based calculated M/N for MA957, and the more recent data on J12YWT, are also lower than those measured by SANS. However, decreasing the APT M/O ratio closer to a stiochiometric value of less than 1 and increasing either the atomic density or Fe content of the NFs, increases the M/N ratio closer to the measure values. Indeed, modest combinations of these adjustments provide reasonable consistency between the APT and SANS results for the commercial vendor alloys. Note, that precise APT measurement of the dominant matrix element (Fe) content of nm-scale features is difficult, since this depends on the interface structure and how the cluster boundary is located in the APT data analysis. While the APT S/O and Ti/Y ratios should be reliable, if present, oxides are non-conducting phases and variations in the field emission processes may perturb the measured atomic ratios. Further, the interpretation of M/N ratios from SANS studies is complicated by a number of factors, including the assumptions made in defining a control alloy (e.g., 14WT for 14YWT).

Transmission electron microscopy (TEM) studies have shown the presence of nm-scale features down to about 2 nm diameter or smaller [2,3,9,11,21-23]. The association of these imaged features with Y-Ti-O enriched and Fe depleted regions has been confirmed by energy filtered TEM (EFTEM) [22]. While EFTEM resolution limits are as low as 1 nm for very thin foils, but typically ≈ 2-3 nm, and interpretation of the TEM results has been complicated by specimen preparation challenges, like artifacts produced by ion milling and FIBing, as well as surface deposits formed during electropolishing. Notably, TEM studies of somewhat larger NF (> 5 - 7 nm) in alloys similar to those studied in this work have confirmed the presence of $Y_2Ti_2O_7$ pyrochlore and Y_2TiO_5 oxides [3,9,11,18,20].

Thus additional work will be needed to clarify the nature and composition of the NFs over a range of sizes, using a variety on advanced high-resolution microanalytical tools. However the current state of understanding of the character of the NFs can be summarized as follows.

1. SANS data for extruded alloys (and fast annealed powders described in detail elsewhere) are consistent with the formation of nm-scale complex oxides like Y_2TiO_3 and $Y_2Ti_2O_7$. These are also likely candidates for the small NFs found in TEM studies, although this will require further confirmation. At larger sizes, TEM studies have clearly identified the presence of complex oxides.

2. Taken at face value, the M/O and S/O ratios that are greater than 1 found in APT studies are not consistent with known complex oxides. Further, the corresponding Ti/Y ratios are much larger than expected for any oxide phase. These NFs may be non-equilibrium sub-oxide transition phases.

3. NFAs that are produced by HIPing, with a slow heat up period, contain larger volume fractions of NFs at lower nominal consolidation temperatures and generally have higher M/N ratios than alloys that are rapidly heated. This is tentatively attributed to a significant Fe content in the NF (25 to 35%) that may be due to precipitation at lower temperatures during heat up. These NFs may also be non-equilibrium sub-oxide transition phases, or even coherent solute enriched zones.

4. Resolution of the character and composition of various NFs will require additional research.

Concluding Remarks

This study provided significant insight on the sequence of events leading to the formation of NFs in MA, hot consolidated ferritic stainless steels. Yttria is dissolved in the metallic powders during MA. The dissolved Y and O, and when present Ti, precipitate during hot consolidation. The N and f of NFs decrease, and their r increase, with higher consolidation temperatures. At 850 and 1000°C, the NFs form in both attritor and SPEX milled alloys with Y, both with and without Ti additions. SPEX milling produces higher volume fractions of NFs and higher hardness in these cases. The presence of Ti refines the NFs, and both Ti and Y as well as high milling energy are necessary for the formation NFs at the highest consolidation temperatures of 1150°C. The microhardness of the consolidated alloys also track the effects of the compositional and processing variables on the NFs. However, the precise structures and compositions of the NFs are still not well understood. The varied character of the NFs depends on the alloy composition and processing variables and, in alloys with Y and Ti, the smallest NFs appear to range from coherent solute enriched zones, or sub-oxide particles, to complex oxide phases.

Acknowledgements
The research carried out in our work was built on the pioneering contributions of J. Fisher (INCO), the inventor of MA NFAs, as well as that of both Dr. M. Hamilton (PNNL) and her co-workers in the US Breeder Reactor Materials Program and Professor S. Ukai (currently at Hokkaido University) and his collaborators in Japan. The authors gratefully acknowledge Doug Klingensmith (UCSB) for his contributions to the SANS measurements, Professor Brian Wirth (UC Berkeley) for his help in analysis of the SANS data and both Dr. Mike Miller and Kaye Russell for their guidance the APT studies. We acknowledge the support of the National Institute of Standards and Technology, US Department of Commerce, Center for Neutron Research in providing the SANS facilities used in this work. Research at the Oak Ridge National Laboratory SHaRE User Center was sponsored by the Division of Materials Sciences, U.S. Department of Energy (DOE), under contract DE-AC05-00OR22725 with UT-Battelle, LLC. The overall research effort at UCSB was supported by DOE Office of Fusion Energy Science (Grant # DE-FG03-94ER54275) and the I-NERI DOE Office of Nuclear Energy through a subcontract with ORNL (Grant # 400014112).

References

1. J. J. Fisher, “Dispersion Strengthened Alloys for Use in Breeder Reactors”, US Patent Number 4,075,010 (1978)
2. M. L. Hamilton, D. S. Gelles, R. J. Lobsinger, G. D. Johnson, W. F. Brown, M. M. Paxton, R. J. Puigh, C. R. Eiholzer and M. A. Blotter, “Fabrication Technological Development of the Oxide Dispersion Strengthened Alloy MA957 for Fast Reactor Applications”, PNNL-13168 (1991, released 2000)
3. S. Ukai, M. Harada, H. Okada, M. Inoue, S. Nomura, S. Shikakura, K. Asabe, T. Nishida and M. Fujiwara, “Alloying Design of Oxide Dispersion Strengthened Ferritic Steel for Long Life FBRs Core Materials”, J. Nucl. Mater., 204(1993) 65-73.
4. S. Ukai, T. Nishida and H. Okada: “Development of Oxide Dispersion Strengthened Steels for FBR Core Application, (I) Improvement of Mechanical Properties by Recrystallization Processing”, J. Nucl. Sci. Technol., 34-3 (1997) 256-63.
5. S. Ukai, T. Nishida, T. Okuda and T. Yoshitake, “Development of Oxide Dispersion Strengthened Steels for FBR Core Application, (II) Morphology Improvement by Martensite Transformation”, J. Nucl. Sci. Technol., 35(1998) 294-300.
6. S. Ukai, T. Nishida, T. Okuda and T. Yoshitake, “R&D of Oxide Dispersion Strengthened Ferritic Martensitic Steels for FBR”, J. Nucl. Mater., 258-63 (1998) 1745-49.
7. S. Ukai, T. Yoshitake, S. Mizuta, Y. Matsudaira, S. Hagi and T. Kobayashi, “Preliminary Tube Manufacturing of Oxide Dispersion Strengthened Ferritic Steels with Recrystallized Structure”, J. Nucl. Sci. Technol., 36 (1999) 710-712.

8. S. Ukai, S. Mizuta, T. Yoshitake, T. Okuda, M. Fujiwara, S. Hagi and T. Kobayashi, “Tube Manufacturing and Characterization of Oxide Dispersion Strengthened Ferritic Steels”, J. Nucl. Mater., 283-287 (2000) 702-706.
9. S. Ukai, T. Okuda, M. Fujiwara, T. Kobayashi, S. Mizuta and H. Nakashima, “Characterization of High Temperature Creep Properties in Recrystallized 12Cr-ODS Ferritic Steel Claddings”, J. Nucl. Sci. Technol., 39(8) (2002) 872-879.
10. S. Ukai and M. Fujiwara, “Perspective of ODS Alloys Application in Nuclear Environments”, J. Nucl. Mater., 307-311 (2002) 749-757.
11. S. Yamashita, S. Ohtsuka, N. Akasaka, S.Ukai, and S. Ohnukiy, “Formation of Nanoscale Complex Oxide Particles in Mechanically Alloyed Ferritic Steel”, Phil. Mag. Lett., 84 (8) (2004) 525-529.
12. S. Ohtsuka, S. Ukai, M. Fujiwara, T. Kaito and T. Narita, “Nano-structure Control in ODS Martensitic Steels by Means of Selecting Titanium and Oxygen Contents”, J. Phys. Chem. Solids, 66 (2005) 571-575.
13. H. Sakasegawa, S. Ohtsuka, S. Ukai, H. Tanigawa, M. Fujiwara, H. Ogiwara and A. Kohyama, “Microstructural Evolution During Creep of 9Cr-ODS Steels”, Fusion Eng. Des., 81 (2006) 1013-1018.
14. S. Ohtsuka, S. Ukai, H. Sakasegawa, M. Fujiwara, T. Kaito and T. Narita, “Nano-mesoscopic Structural Characterization of 9Cr-ODS Martensitic Steel for Improving Creep Strength”, J. Nucl. Mater. (2007), doi:10.1016/j.jnucmat.2007.03.004.
15. T. Okuda and M. Fujiwara, “Dispersion Behavior of Oxide Particles in Mechanically Alloyed ODS Steel”, J. Mater. Sci. Let., 14 (1995) 1600-1603.
16. R. Schaeublin, T. Leguey P. Spatig, N. Baluc and M. Victoria, “Microstructure and Mechanical Properties of Two ODS Ferritic/Martensitic Steels”, J. Nucl. Mater., 307-311 (2002) 778.
17. M. Klimiankou, R. Lindau and A. Moslang, “HRTEM Study of Yttrium Oxide Particles in ODS Steels for Fusion Reactor Application”, J. Cryst. Growth 249 (2003) 381-87.
18. M. Klimiankou, R. Lindau, A. Moslang, “TEM Characterization of Structure and Composition of Nanosized ODS Particles in Reduced Activation Ferritic-Martensitic Steels”, J. Nucl. Mater., 329-333 (2004) 347-351.
19. H. Kishimoto, M. J. Alinger, G. R. Odette and T. Yamamoto: “TEM Examination of Microstructural Evolution during Processing of 14CrYWTi Nanostructured Ferritic Alloys”, J. Nucl. Mater., 329-33 (2004) 369-71.
20. M. Klimiankou, R. Lindau and A. Moslang, “Energy-filtered TEM Imaging and EELS Study of ODS Particles and Argon-Filled Cavities in Ferritic-Martensitic Steels”, Micron, 36 (2005) 1-8
21. R. Coppola, M. M. Klimiankou, R. Lindau, R. P. May and M. Valli, “SANS and TEM Study of Particle Distributions in Oxide-Dispersion Strengthened Eurofer Martensitic Steel for Fusion Reactors”, Physica B 350 (2004) e545-e548.
22. T. Yamamoto, G.R. Odette, P. Miao, D.T. Hoelzer, J. Bentley, N. Hashimoto, H. Tanigawa and R.J. Kurtz, “The transport and Fate of Helium in Nanostructured Ferritic Alloys At Fusion Relevant He/dpa Ratios and dpa Rates”, J. Nucl. Mater. (2007), doi:10.1016/j.jnucmat.2007.03.047.
23. P. Miao, G. R. Odette, T. Yamamoto, M. Alinger and D. Klingensmith, “Thermal Stability of Nano-structured Ferritic Alloy”, accepted by J. Nucl. Mater.
24. D.S. Gelles, “Microstructural Examination of Commercial Ferritic Alloys at 200 dpa”, J. Nucl. Mater., 233-237 (1996) 293-298.
25. M.B. Toloczko, F.A. Garner an C.R. Eiholzer, “Radiation Creep of Various Ferritic Alloys Irradiated at 400ºC in the PFR and FFTF Reactors”, J. Nucl. Mater., 258-263 (1998) 1163-1166.
26. J. Saito, T. Suda, S. Yamashita, S. Ohnuki, H. Takahashi, N. Akasaka, M. Nishida and S. Ukai, “The Effect of Mechanical Alloying Parameters on Irradiation Damage in Oxide Dispersion Strengthened Ferritic Steels”, J. Nucl. Mater., 283-287 (2000) 647-651.
27. S. Yamashita, S. Watanabe, S. Ohnuki, H, Takahashi, N. Akasaka and S. Ukai, “Phase Stability of Oxide Dispersion-Strengthened Ferritic Steels in Neutron Irradiation”, J. Nucl. Mater., 307-311(2002) 283-88.
28. V. V. Sagaradze, V. I. Shalaev, V. L. Arbuzov, B. N. Goshchitskii, Y. Tian, W. Qun, and S. Jiguang, “MicroMartensitic Steels”, J. Nucl. Mater., 329-333 (2004) 1053-1056.

29. S. Yamashita, N. Akasaka and S. Ohnuki, “Nano-oxide Particle Stability of 9-12Cr Grain Morphology Modified ODS Steels Under Neutron Irradiation”, J. Nucl. Mater., 329-333 (2004) 377-381.
30. H. Kishimoto, K. Yutani, R. Kasada and A. Kimura, “Helium Cavity Formation Research on Oxide Dispersion Strengthening (ODS) Ferritic Steels Utilizing Dual-Ion Irradiation Facility”, Fusion Eng. Des., 81 (2006) 1045-1049.
31. P. Pareige, M.K. Miller, R.E. Stoller, D.T. Hoelzer, E. Cadel, B. Radiquet, “Stability of Nanometer-Sized Oxide Clusters in Mechanically-Alloyed Steel under Ion-Induced Displacement Cascade Damage Conditions”, J. Nucl. Mater., 360(2007) 136 - 142.
32. D.J. Larson, P.J. Maziasz, I-S. Kim and K. Miyahara, “Three-Dimensional Atom Probe Observation of Nanoscale Titanium-Oxygen Clustering in an Oxide-Dispersion-Strengthened Fe-12Cr-3W-0.4Ti + Y_2O_3 Ferritic Alloy”, Scripta Mater. 44 (2001) 359–364.
33. M. K. Miller, E. A. Kenik, K. F. Russell, L. Heatherly, D. T. Hoelzer and P. J. Maziasz, “Atom Probe Tomography of Nanoscale Particles in ODS Ferritic Alloys”, Mater. Sci. Eng. A-Struct., 353(2003) 140-45.
34. M.K. Miller, D.T. Hoelzer, E.A. Kenik, K.F. Russell, “Nanometer Scale Precipitation in Ferritic MA/ODS Alloy MA957”, J. Nucl. Mater., 329-333 (2004) 338-341.
35. M. K. Miller, D. T. Hoelzer, E. A. Kenik and K. F. Russell, “Stability of Ferritic MA/ODS Alloys at High Temperatures”, Intermetallics, 133-4(2005) 387-392.
36. M. K. Miller, K. F. Russell and D. T. Hoelzer, “Characterization of Precipitates in MA/ODS Ferritic Alloys”, J. Nucl. Mater., 351(2006) 261-268.
37. M. J. Alinger, G. R. Odette and D. T. Hoelzer, “The Development and Stability of Y–Ti–O Nanoclusters in Mechanically Alloyed Fe–Cr Based Ferritic Alloys”, J. Nucl. Mater., 329-33(2004) 382-86.
38. M.J. Alinger, “*On the Formation and Stability of Nanometer Scale Precipitates in Ferritic Alloys During Processing and High Temperature Service*”, Ph.D. Thesis, University of California, Santa Barbara, 2004.
39. A. Alamo, V. Lambard, X. Averty and M.H. Mathon, “Assessment of ODS-14%Cr Ferritic Alloy for High Temperature Applications”, J. Nucl. Mater., 329–333 (2004) 333–337.
40. R.L. Klueh, J.P. Shingledecker, R.W. Swindeman and D.T. Hoelzer, “Oxide Dispersion-Strengthened Steels: A Comparison of Some Commercial and Experimental Alloys”, J. Nucl. Mater., 341 (2005) 103-114.
41. M. S. El-Genk and J.–M. Tournier, “A Review of Refractory Metal Alloys and Mechanically Alloyed-Oxide Dispersion Strengthened Steels for Space Nuclear Power Systems”, J. Nucl. Mater., 340 (2005) 93-112.
42. JCPDS, Powder Diffraction File, International Center for Diffraction Data, 1601 Park Lane, Swarthmore, PA 19081 - 2389 (1990).
43. N. Mizutani, Y. Tajima and M. Kato, “Phase Relations in the System Y_2O_3 – TiO_2”, J. Am. Ceram. Soc. 59 (1976) 168-171.
44. E. Ma, M. Atzmon, F.E. Pinkerton, “Thermodynamic and Magnetic Properties of Metastable Fe_xCu_{100-X} Solid Solutions Formed by Mechanical Alloying”, J. Appl. Phys. 74-2 (1993) 955-962.
45. H. K. D. H. Bhadeshia, “Mechanically Alloyed Metals”, Mater. Sci. Tech., 16 (2000) 1404-11.
46. G. Kostorz, *Neutron Scattering*, Academic Press, New York (1979).
47. E. Mader, “*Kinetics of Irradiation Embrittlement and the Post-Irradiation Annealing of Nuclear Reactor Pressure Vessel Steels*”, Ph.D. Thesis, University of California, Santa Barbara (1995).
48. M. K. Miller: *Atom Probe Tomography: Analysis at the Atomic Level*, Kluwer Academic / Plenum Publishers, New York (2000) 239.
49. H.P. Klug and L.E. Alexander, X-Ray Diffraction Procedures, John Wiles and Sons, Inc., New York, NY (1974).
50. M. K. Miller, personal communication.